Hyperfine Interactions 125 (2000) 69–90

Techniques for inelastic X-ray scattering with μeV-resolution

R. Röhlsberger

Universität Rostock, Fachbereich Physik, August-Bebel-Str. 55, D-18055 Rostock, Germany

A new spectroscopic technique is introduced that allows tuning of a μeV-wide beam of synchrotron radiation over a range of a few meV. It relies on nuclear resonant scattering that is subject to the Doppler effect in high speed rotary motion. Two mechanisms are discussed how to extract the resonantly scattered radiation out of the broad band of synchrotron radiation: (a) grazing incidence reflection from a rotating disk in combination with a polarization filtering technique and (b) deflection of resonantly scattered radition via the recently discovered Nuclear Lighthouse Effect. Implications for inelastic X-ray scattering and elastic nuclear resonant scattering are discussed.

Keywords: X-ray spectroscopy, nuclear resonant scattering, Doppler effect

1. Introduction

The availability of high-brilliance, undulator-based synchrotron radiation sources has pushed forward the development of inelastic X-ray scattering techniques with very high energy resolution [1]. Presently, vibrational excitations in solids and liquids are studied with meV-resolution by using backscattering monochromators and analyzers [2–6]. While this method uses coherent inelastic scattering to determine the dispersion of vibrational excitations in condensed matter, a new technique was recently introduced to measure the vibrational density of states via incoherent inelastic nuclear resonant scattering [7–10]. This method relies on detection of time-delayed fluorescence photons emitted by decaying Mössbauer nuclei that were excited by synchrotron radiation, i.e., resonant nuclei in the sample are used as energetic analyzers. The yield of those fluorescence photons as a function of energy gives a direct measure of the vibrational density of states of the ^{57}Fe atoms in the sample. Energy resolutions of a few meV are routinely achieved in this kind of spectroscopy by employing subsequent high-order reflections in dispersive geometry [11]. Recently, values in the sub-meV range have been reached by using extremely asymmetric high-order reflections [12,13]. The principal limit of that method is reached when the asymmetry angle approaches the Bragg angle, so that total external reflection takes place and the reflectivity of the Bragg reflection drops. Therefore the minimum bandwidth that can reasonably be obtained in the hard X-ray regime is limited to a few hundred μeV. Consequently, there is currently no X-ray spectroscopic technique available that covers the range

from a few μeV to a few meV with μeV resolution. On the other hand, vibrational excitations in this energy range have recently attracted considerable attention. For instance, vibrational spectra of disordered solids exhibit a universal feature in the range of 1–10 meV, the so-called boson peak, its origin still being the subject of debate [14]. Further examples are magnons, two-level systems, phasons in quasicrystals, rotational excitations in liquids, soft phonons, etc.

The energy bandpass and the tunability in presently existing inelastic X-ray scattering techniques are determined by the laws of electronic Bragg diffraction from (im)perfect single crystals. Energy resolutions that go significantly below 1 meV require a qualitatively different scattering mechanism. In this contribution we show how this can be achieved by *elastic nuclear resonant scattering*, the various aspects of which are extensively reviewed in this issue. We introduce a novel class of X-ray spectrometers that provide a μeV bandpass together with a tunability over several meV.

Here we will concentrate on the 14.4 keV resonance of ^{57}Fe with a natural linewidth of $\Gamma_0 = 4.7$ neV. An *energy tuning* can be achieved by Doppler motion of either the radiation source or the absorbing sample. In case of ^{57}Fe, a velocity of 100 ms^{-1} corresponds to an energy shift of 4.7 meV. Such velocities cannot be conveniently realized in linear motion, but they can easily be reached in rotary motion. Therefore, the spectrometers described here are based on high speed rotary motion for energy tuning of the radiation. The energy bandwidth of the resonantly scattered radiation is determined by the magnitude of level splitting due to hyperfine interactions and dynamical effects of multiple scattering like speedup of the nuclear decay. In case of ^{57}Fe, the *energy bandwidth* can be broadenend up to more than 0.5 μeV.

This article is organized as follows: First, as the theoretical basis, we discuss the principles of nuclear resonant scattering from fast rotating samples. As a result of this, two different concepts for a spectrometer with μeV resolution and meV-tunability will emerge. In the first type of spectrometer, nuclear resonant scattering takes place in grazing incidence geometry at a ^{57}Fe-coated mirror rotating with frequencies of up to 150 Hz. Very efficient background suppression is achieved by employing a polarization filtering technique. The second type of spectrometer employs forward scattering from a ^{57}Fe foil that is rotating with frequencies of several kHz. Here the resonantly scattered radiation is separated from the nonresonant background by the "Nuclear Lighthouse Effect": during its lifetime, the nuclear exciton is carried with the rotating foil and reemission proceeds into the rotated direction [15].

In both cases we discuss the scattering mechanism in detail, especially with respect to the energy bandwidth and photon flux to be expected. After description of the instrumentation first experimental results are presented. On the basis of these results, the performance of these spectrometers in future inelastic scattering experiments will be discussed.

2. Nuclear resonant scattering from a rotating medium

The formation of a nuclear exciton by a synchrotron radiation pulse with wavevector $\vec{k}_0$ creates a collective phasing of the nuclei that is preserved during the lifetime of the exciton. Coherence leads to remarkable properties of the exciton decay, notably the speedup of the radiative decay compared to that of an isolated nucleus, and quantum beats resulting from interference of waves emitted from different resonances at different nuclei [16]. In the following we denote this time dependence by $\vec{A}_0(t)$, representing the photon potential of the scattered radiation. In case of a homogeneous sample at rest, the dependence of the photon potential on spatial coordinates is described by

$$\vec{A}(\vec{r},t) = \exp\{\mathrm{i}\vec{k_0}\cdot\vec{r}\}\vec{A}_0(t). \tag{2.1}$$

The spatial phasing introduces a strongly directional dependence of the coherent radiative decay, which proceeds in the forward direction (for any sample) or diffraction directions if a Bragg condition is fulfilled (for crystals).

We now assume the sample to be rotating with angular frequency $\vec{\Omega}$. Due to conservation of angular momentum, the photon potential acquires in first approximation an additional dynamic phase factor, resulting from the rotation of the nuclear exciton during its lifetime [15]:

$$\vec{A}(\vec{r},t) = \exp\{\mathrm{i}\vec{J}\cdot\vec{\Omega}t/\hbar\}\exp\{\mathrm{i}\vec{k}_0\cdot\vec{r}\}\vec{A}_0(t), \tag{2.2}$$

where t is the time after excitation and $\vec{J}=\vec{L}+\vec{S}$ is the total angular momentum of the excited nuclear state, consisting of orbital angular momentum $\vec{L}=\hbar\vec{r}\times\vec{k}_0$ and spin angular momentum $\vec{S}$ [17]. The spin operator $\vec{S}$ acts on the components of $\vec{A}(\vec{r})$ without changing its $\vec{r}$ dependence, i.e., it leads to a rotation of the polarization state of the photon field. Since this effect has no influence on the experiments described here, it will be neglected. The phase can now be rewritten as

$$\vec{J}\cdot\vec{\Omega}t/\hbar = \left(\vec{r}\times\vec{k}_0\right)\cdot\vec{\Omega}t = \left(\vec{k}_0\times\vec{\Omega}t\right)\cdot\vec{r}, \tag{2.3}$$

where we have used the vector identity $(\vec{a}\times\vec{b})\cdot\vec{c}=(\vec{b}\times\vec{c})\cdot\vec{a}$. The evolution of the nuclear excited state is then given by

$$\vec{A}(\vec{r},t) = \exp\{\mathrm{i}(\vec{k}_0 + \vec{k}_0\times\vec{\Omega}t)\cdot\vec{r}\}\vec{A}_0(t). \tag{2.4}$$

This is a wave that propagates in the direction of $\vec{k}(t) = \vec{k}_0 + \vec{k}_0\times\vec{\Omega}t$, i.e., the rotated state at time t is again an eigenstate of the momentum operator. The scattering geometry is shown schematically in figure 1. The nuclear exciton is carried with the rotating sample and its decay proceeds in the rotated direction. Due to the analogy with a rotating beam of light, this effect was called the "Nuclear Lighthouse Effect" [15]. Due to the unique relationship between the time t after excitation and the momentum transfer $\vec{q}(t) = \vec{k}(t) - \vec{k}_0$, the time evolution of the nuclear decay is mapped to an angular scale, as shown in figure 1. At sufficiently high rotational frequencies and

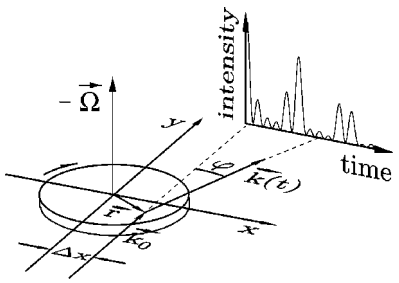

Figure 1. Nuclear resonant scattering from a sample rotating with angular velocity $\vec{\Omega}$. Due to the Nuclear Lighthouse Effect the time spectrum of the nuclear decay is mapped to an angular scale.

a large enough distance from the sample, the resonantly scattered radiation is well separated from the nonresonant direct beam.

As another consequence of the rotational phase factor, in addition to the angular deflection, the energy of the scattered radiation is Doppler shifted relative to the resonance energy. An analysis of the scattering in energy space is easily performed after rewriting the rotational phase in eq. (2.2) as

$$\vec{J}\cdot\vec{\Omega}t/\hbar = \big(\vec{r}\times\vec{k}_0\big)\cdot\vec{\Omega}t = \big(\vec{\Omega}\times\vec{r}\big)\cdot\vec{k}_0 t = \vec{v}\cdot\vec{k}_0 t. \tag{2.5}$$

Fourier transform of eq. (2.4) then results in

$$\vec{A}\big(\vec{r},\omega\big) = \exp\big\{\mathrm{i}\vec{k}\cdot\vec{r}_0\big\}\int \vec{A}_0(t)\exp\big\{\mathrm{i}\big(\omega+\vec{v}\cdot\vec{k}_0\big)t\big\}\mathrm{d}t, \tag{2.6}$$

i.e., the energy of the scattered radiation is Doppler shifted by $\Delta\omega = \vec{v}\cdot\vec{k}_0$. Following the notation and coordinates introduced in figure 1, this Doppler shift is explicitly given by

$$\Delta\omega = \vec{v}\cdot\vec{k}_0 = \Omega k_0 x \quad \text{with} \quad \vec{v} = \vec{\Omega}\times\vec{r} = \begin{pmatrix} -\Omega\, y \\ \Omega\, x \end{pmatrix} \quad \text{and} \quad \vec{k}_0 = \begin{pmatrix} 0 \\ k_0 \end{pmatrix}. \tag{2.7}$$

This means that, at fixed $\vec{\Omega}$, the magnitude of the energy shift is only determined by the transverse displacement x of the scattering position from the center of rotation. An energy tuning can therefore be achieved by variation of x at a constant rotational frequency or by changing the rotational frequency at fixed x.

3. Basic spectrometer design

According to the above section, radiation resonantly scattered from a sample rotating with angular velocity $\vec{\Omega}$ exhibits the following properties:

- *Doppler shift.* The scattering takes place at an energy $E = E_0 - \hbar(\vec{\Omega}\times\vec{r})\cdot\vec{k}_0$, where $\vec{r}$ is the radius vector relative to the center of rotation.
- *Lighthouse Effect.* The wavevector of the scattered radiation is $\vec{k}(t) = \vec{k}_0 + \vec{k}_0\times\vec{\Omega}\,t$.

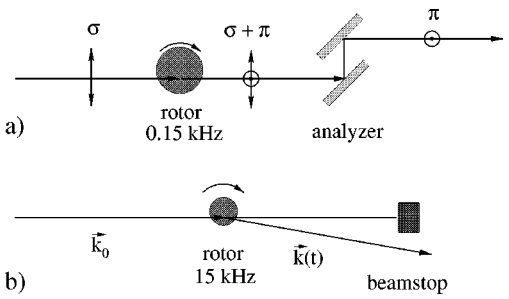

Figure 2. Two schemes to extract a μeV-wide beam, resonantly scattered from a rotating sample, with a tunability over a few meV around the resonance energy. (a) Rotating mirror spectrometer, (b) Lighthouse spectrometer.

Based on these properties, two ways are suggested here how to obtain a μeV wide beam that is tunable over several meV. For that purpose, the resonantly scattered radiation has to be separated from the nonresonant radiation. This can be accomplished by techniques that are sensitive to the unique properties of nuclear resonant scattering, e.g., the time scale of the decay and its polarization characteristics. Polarization components generated as a result of orthogonal scattering (e.g., $\sigma \rightarrow \pi$) can be filtered out by crystal analyzers [18–20]. The properties of magnetic nuclear resonant scattering are summarized in section 4.1. It turns out that the highest throughput can be reached in grazing incidence reflection from magnetized layers. This geometry requires flat mirrors of several cm radius that are coated with a thin film containing the resonant isotope in a ferromagnetic matrix. Due to the large size of these rotors, rotational frequencies are limited to 100–200 Hz. In that case the Nuclear Lighthouse Effect can be (almost) neglected. This approach is shown schematically in figure 2(a).

The second type of spectrometer relies entirely on the time scale of the nuclear decay that manifests itself in the Nuclear Lighthouse Effect. At sufficiently high rotational speeds, the resonantly scattered radiation is spatially separated from the nonresonant background which can be blocked out by placing a beam stop at the primary beam, see figure 2(b). No high-resolution crystal optics is necessary. The high rotational frequencies of a few kHz imply small rotor diameters. Therefore, grazing incidence reflection is not appropriate in this case. Instead, forward scattering from an unmagnetized sample has to be employed.

4. Spectrometer characteristics

4.1. Magnetic nuclear resonant scattering

Nuclear resonant scattering in the presence of magnetic hyperfine interactions exhibits optical activity with strong orthogonal scattering, e.g., from incident σ-polarization into π-polarization. Since this optical activity occurs only in the vicinity

of the nuclear resonance, an ultranarrow monochromatization of synchrotron radiation is possible if the π-polarization can be extracted by a polarization filtering technique. The choice of the material and the magnetization geometry determine the integrated intensity T of $\sigma \rightarrow \pi$ scattering. The magnitude of T finally determines the photon flux on the sample under study. Therefore, it is an important figure-of-merit for optimization of a spectrometer. We define T by

$$T = \int_{-\infty}^{\infty} \left| A_{\sigma\pi}(\omega) - A_0 \right|^2 \mathrm{d}\omega, \tag{4.1}$$

where $A_{\sigma\pi}$ is the amplitude of $\sigma \rightarrow \pi$ scattering, and A_0 is the amplitude scattered off-resonance. An alternative criterion is the intensity of delayed quanta measured in a certain time interval:

$$T_t = \int_{t_1}^{t_2} \left| A_{\sigma\pi}(t) \right|^2 \mathrm{d}t. \tag{4.2}$$

Both expressions are equivalent for $t_1 = 0^+,\ t_2 = \infty$. Equation (4.2) is more appropriate if certain regions of the time spectrum are excluded from detection, e.g., in the presence of strong prompt electronic (charge) scattering. It will be used for evaluation of the Nuclear Lighthouse Effect in section 4.2.2.

The purpose of this section is to discuss various scattering geometries with respect to the value of T that can be obtained. As a general rule, the maximum values of T are obtained for scattering from ferromagnetic samples that are magnetized parallel to $\vec{k}_0$ (Faraday geometry). In this case, the nondiagonal elements of the scattering matrix are largest [20,21]. Then the circular polarizations are eigenpolarizations of the sample and incident linear polarization experiences strong orthogonal scattering.

4.1.1. Forward scattering

The Faraday geometry is not well suited for forward scattering through thin foils. Due to the strong magnetic shape anisotropy, fields of several Tesla are required to force the magnetization direction out of plane. An alternative would be to have the magnetization in the plane of the foil that is then tilted relative to the incident beam so that the component parallel to $\vec{k}_0$ becomes effective. In any case, high speed rotary motion within a strong magnetic field would cause considerable heating of the sample due to eddy currents and therefore has to be excluded here. However, this scheme could be attractive for Doppler tuning employing linear motion. To give a brief overview, T has been calculated for the two magnetization geometries where the strongest polarization mixing effects occur: the already mentioned Faraday geometry and the "45°-geometry", where $\vec{B}$ is perpendicular to $\vec{k}$, and inclined by 45° relative to the vector of the incident linear polarization. The result is displayed in figure 3. T depends strongly on the lower boundary t_1 of the time window. For $t_1 = 0^+$ in eq. (4.2), the Faraday geometry (a,b) yields the largest value of T. On the other hand, if t_1 = 10 ns, the 45°-geometry (b,c) is more advantageous.

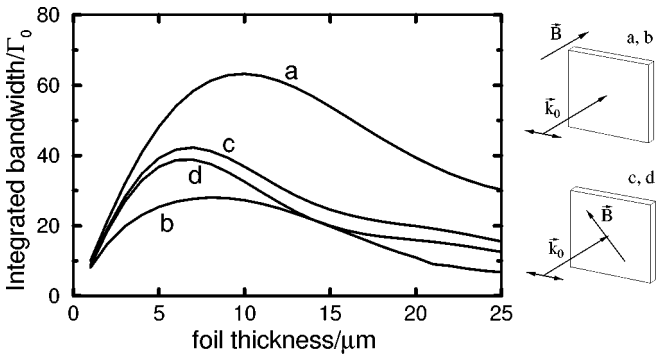

Figure 3. Thickness dependence of the integrated delayed intensity T (eq. (4.1)) of polarization-mixing forward scattering through a ^{57}Fe foil in two magnetization geometries shown on the right: $\vec{B} \parallel \vec{k}_0$ (Faraday geometry) and $\vec{B} \perp \vec{k}_0$ with $\Theta(\vec{B},\vec{\sigma}) = 45°$, where $\vec{\sigma}$ indicates the linear polarization state of the incident radiation. The curves are calculated according to eq. (4.2) with $t_1 = 0^+$ (a), (c) and $t_1 = 10$ ns (b), (d). The energetic bandwidth is measured in units of the natural linewidth $\Gamma_0 = 4.7$ neV of the ^{57}Fe resonance.

4.1.2. Grazing incidence reflection

The Faraday magnetization geometry can be easily realized in grazing incidence geometry with thin ferromagnetic films. Fields of a few mT are sufficient to achieve a complete in-plane magnetization of the film. For the theoretical treatment of polarization mixing scattering in grazing incidence geometry, see, e.g., [21,22]. For various layer systems, T has been plotted as a function of angle of incidence, see figure 4. The largest values of T are obtained if the ^{57}Fe layer is coated on a total reflecting substrate layer, i.e., a layer of higher electron density, because the radiation then passes the ^{57}Fe at least twice. This becomes evident from comparison with a single ^{57}Fe layer coated directly on a substrate of lower electron density. In this case T assumes a maximum value of $30\,\Gamma_0$ at $\varphi = 3.8$ mrad, the electronical critical angle of Fe (a). Values more than twice as large are calculated for 10 nm ^{57}Fe coated on Pd, where $T = 65\,\Gamma_0$ is reached at $\varphi = 4.2$ mrad, close to the critical angle of Pd (b). In general, large values for T are found if the ^{57}Fe is coated on a substrate with a high reflectivity. This can also be a multilayer with the angle of incidence adjusted to one of its Bragg peaks. As an example, a multilayer consisting of $40 \times$ (1.5 nm Mo/2.5 nm Si) has been assumed with 30 nm ^{57}Fe coated on top of it. In this case, $T = 55\,\Gamma_0$ is achieved at $\varphi = 11$ mrad (c). Such a solution becomes attractive in the case that a large beam cross section has to be reflected. The largest value of T was found for a Pd/C/Pd X-ray waveguide structure, where a 3.5 nm thick ^{57}Fe layer was embedded in the center of the C spacer layer, so that the actual layer sequence (as seen from the top) was 2 nm Pd/10 nm C/3.5 nm ^{57}Fe/10 nm C/Pd. At a certain angle, a guided mode inside the waveguide is excited. The radiation is reflected several times at the internal C/Pd boundaries and constructive interference between all these waves leads to a strong intensity buildup inside the spacer layer [23–25]. Here a value of $T = 78\,\Gamma_0$ is reached at $\varphi = 2.2$ mrad (d). In this case, however, it is questionable whether such a

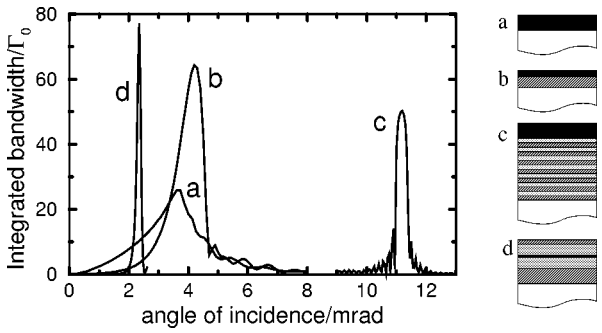

Figure 4. Rocking curves of the energy integrated reflectivity $|R_{\sigma\pi}|^2$ of various layer systems: (a) 30 nm ^{57}Fe, (b) 10 nm ^{57}Fe on Pd, (c) 40 nm ^{57}Fe on a Mo/Si multilayer with $d_{\mathrm{Si}} + d_{\mathrm{Mo}} = 4$ nm, (d) 3.5 nm ^{57}Fe embedded in the center of a Pd/C/Pd waveguide structure. The energetic bandwidth is measured in units of the natural linewidth $\Gamma_0 = 4.7$ neV of the ^{57}Fe resonance.

layer system can be produced, since very smooth boundaries are required. Moreover, it has to be ensured that the thin ^{57}Fe layer is ferromagnetic even if diffusion of C into the Fe may take place. For that reason, the most simple layer system with a T value close to the maximum has been chosen for the rotating-mirror spectrometer, i.e., 11 nm ^{57}Fe on a Pd substrate layer (b).

4.2. Background suppression

4.2.1. Polarization filtering

The basic idea to separate the nuclear resonant $\sigma \rightarrow \pi$ scattering from the nonresonant polarization conserving scattering is to use two polarizing reflections in crossed setting with the resonant scattering process in between. The first crystal generates almost pure σ-polarization. The second crystal is adjusted so that its scattering plane is at an angle of 90° with that of the first crystal. Then the polarization state transmitted by the first crystal is almost completely blocked while the $\sigma \rightarrow \pi$ scattering is transmitted. This scheme resembles the principle of optical polarimetry, where the optical activity of a substance is measured in a polarizer/analyzer setup.

Visible light can be polarized by reflection from a dielectric mirror under the Brewster angle. In this case the reflected and the diffracted beam enclose an angle of 90°. Due to the dipole emission characteristic, no radiation is reflected that is polarized parallel to the scattering plane. Only those components are reflected that are polarized perpendicular to the scattering plane (σ-polarization). The same principle can be used for X-rays by using Bragg reflections with Bragg angles of 45°. This is the Brewster angle for X-rays since diffraction effects are negligible at these energies. However, due to the fixed lattice-plane spacing of single crystals, it is very unlikely to find a reflection with a Bragg angle of exactly 45° for a given wavelength of a nuclear transition. The deviation from 45° determines the suppression ratio of π-polarization relative to σ-polarization. At 14.4 keV the Si(8 4 0) reflection with $\Theta_{\mathrm{B}} = 45.1°$ is most suited to be used for a polarizing Bragg reflection [18–20,26]. A disadvantage

is the small Darwin width of 0.5 μrad that limits the angular acceptance. This value can be enlarged to 10.6 μrad by cutting the crystal with an asymmetry angle of 43.1°, i.e., the angle of incidence relative to the crystal surface is 2° [18,20,26]. Due to this small angular acceptance, experiments with such polarizing reflections can be efficient only at high-brilliance synchrotron radiation sources. Typical divergences at undulator beamlines of 3rd generation facilities are in the range of 15 μrad vertical and 50 μrad horizontal. Despite such a good collimation, there is still a mismatch with the angular acceptance of the polarizer/analyzer crystals, so that only a flux of approximately 10% of the incident flux can be used.

Formally, the transmission through an arrangement of two crossed linear polarizers with an intermediate polarization mixing scattering process is described in the linear polarization basis (σ, π) by the following expression:

$$(A_\sigma, A_\pi) = (1, \xi) \begin{pmatrix} 1 & 0 \\ 0 & \delta \end{pmatrix} \begin{pmatrix} R_{\sigma\sigma} & R_{\sigma\pi} \\ R_{\pi\sigma} & R_{\pi\pi} \end{pmatrix} \begin{pmatrix} \delta & 0 \\ 0 & 1 \end{pmatrix} \approx (\delta\, R_{\sigma\sigma}, R_{\sigma\pi}). \qquad (4.3)$$

This is the description of the setup within the Jones-matrix formalism. The radiation from the undulator is almost completely σ-polarized with a small admixture ξ of π-polarization. The polarizer/analyzer crystals are represented by the corresponding matrices for linear polarizers with an imperfection of $\delta \approx 10^{-4}$–10^{-5}, resulting from the deviation of the Bragg angle from the optimum value of 45°. The middle matrix represents the reflectivity matrix $\widehat{R}$ of the layer system [21].

4.2.2. Lighthouse filtering

Here the separation of the resonantly scattered radiation proceeds via the angular deflection of the delayed quanta. The mapping of the time spectra to an angular scale can be described most conveniently by transition into reciprocal space. In deriving eq. (2.4) we have assumed an incident plane wave, characterized by a unique wavevector $\vec{k}_0$ and full coherence over the sample volume. Due to the finite source size in a real experiment, however, each point of the sample is illuminated by incident waves spread over a range of directions. (We still assume monochromatic radiation.) As a consequence, the degree of coherence between two points of the electromagnetic field at the sample position decreases with increasing transverse separation $\vec{r}_t$. This functional dependence is described by the mutual coherence function $W(\vec{r}_t)$ [27]. The scattered field in reciprocal space is then given by

$$\vec{A}(\vec{q}, t) = \vec{A}_0(t) \int \exp\{\mathrm{i}(\vec{q} - \vec{k}_0 \times \vec{\Omega} t) \cdot \vec{r}\} W(\vec{r}_t)\, \mathrm{d}\vec{r}. \qquad (4.4)$$

In one dimension, $W(\vec{r}_t)$ is often described by a Gaussian with standard deviation ξ, which is then taken as definition of the transverse coherence length. Then we obtain

$$\vec{A}(\varphi, t) = \vec{A}_0(t) \exp\left\{ -\frac{1}{2} k_0^2 \xi^2 (\varphi - \Omega t)^2 \right\}, \qquad (4.5)$$

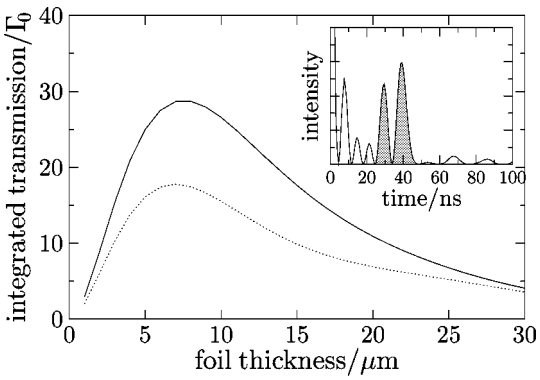

Figure 5. Thickness dependence of the time integrated intensity T_t (eq. (4.2)) of a ^{57}Fe foil: (a) in the time interval 24–46 ns (shaded area in the insert), and (b) in the time interval 34–46 ns.

where we have set $|\vec{q}| = k_0\varphi$, with $\varphi \ll 1$ the scattering vector. Basic considerations about transverse coherence show that $\xi \approx D/(Sk_0)$, where D is the source–sample distance and S is the transverse linear dimension of the source [28,29]. $\Theta_s := S/D$ can be taken as the angle that the source subtends at the sample position. Typical values at insertion devices of third generation synchrotron radiation sources are $\Theta_s \approx 10^{-5}$ and $\xi \approx 10$ μm at X-ray energies of about 10 keV. The mapping of the intensity to an angular scale is obtained by taking the modulus of eq. (4.5) and integrating over the time dependence:[1]

$$I(\varphi) = \int_0^\infty \left|\vec{A}_0(t)\right|^2 \exp\left\{-\frac{(t-\varphi/\Omega)^2}{(\Theta_s/\Omega)^2}\right\} \mathrm{d}t. \tag{4.6}$$

In order to achieve an equivalent time resolution Δt that is comparable to that of existing detectors, the rotational frequency has to be sufficiently high. To obtain a clear angular separation of events that are a time Δt apart, the rotational frequency Ω has to exceed $\Theta_s/\Delta t$. For Δt = 1 ns this leads to the condition $\Omega > 10$ kHz. Such high-speed rotational motion is commonly used in the magic-angle-spinning (MAS) technique of solid state NMR [33], as will be described in more detail in section 6.1.

The energy tuning in this case has to be performed by a transverse displacement of the rotor that is operated at a constant speed, so that the deflection of the resonantly scattered radiation is constant. For use of the deflected radiation in a subsequent experiment, a certain angular range, or time interval, respectively, can be gated out by placement of a slit. In case of scattering from a polycrystalline ^{57}Fe foil, the maximum flux has been determined that can be obtained in the most intense quantum beats in the spectrum. Figure 5 displays the thickness dependence of the flux, as defined by eq. (4.2), that is contained in the quantum beats around 30 ns and 40 ns. A maximum

[1] Equation (4.6) can also be used to determine the effective source size of the radiation via the dependence on Θ_s. However, by taking eq. (4.5) as a function of t at constant φ, such studies are already possible at considerably lower rotational frequencies, see [30].

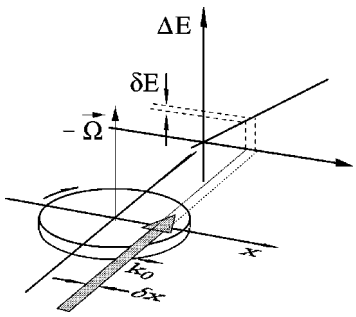

Figure 6. Doppler shift ΔE for resonant reflection from a rotating disk. Due to the linear velocity gradient across the disk, the finite width δx of the incident beam is translated into an energy width δE.

value of T close to $30\,\Gamma_0$ is found for a foil thickness of about 8 μm. T peaks at $17\,\Gamma_0$ if only the quantum beat around 40 ns is taken (dotted line).

4.3. Energy tuning via Doppler shift

Conventional Mössbauer experiments are dealing with recoilless *absorption* of γ-quanta rather than elastic *scattering*, which is absorption and coherent reemission. In the former, either the radiation source or the absorber are in motion, so the conventional Doppler formalism for relative motion between source and absorber can be applied. In case of coherent forward *scattering* from a moving sample, however, the situation deserves a closer inspection.

Consider a monochromatic plane wave $(\omega, \vec{k})$ incident on a bound Mössbauer nucleus moving with velocity $\vec{v}$ relative to the laboratory frame. In the rest frame of the nucleus, its resonance energy is $\hbar\omega_0$, and the plane wave has the frequency $\omega_n = \omega - \vec{v}\cdot\vec{k}$. In order for resonant absorption to take place in this configuration, the incident wave in the lab has to have the frequency $\omega_n = \omega_0 + \vec{v}\cdot\vec{k}$. In the rest frame of the nucleus, the reemitted wave has the frequency ω_0 and the lab frame moves with velocity $-\vec{v}$. Transformation back into the lab frame leads to the frequency ω' of the reemitted wave of $\omega' = \omega_0 - (-\vec{v})\cdot\vec{k}' = \omega_0 + \vec{v}\cdot\vec{k}'$, where $\vec{k}'$ is the direction of reemission. Note that there is an energy transfer of $\Delta E = \vec{v}\cdot(\vec{k} - \vec{k}')$, whereas the Doppler term $\vec{v}\cdot\vec{k}$ corresponds just to a shift of the nuclear absorption energy scale. This result, of course, confirms the result contained in eq. (2.6), but now stands on a more intuitive basis.

Now we want to examine the actual experimental situation. Figure 6 displays the spatial dependence of the Doppler shift for reflection from a rotating mirror that is coated with a resonant isotope. The incident radiation illuminates a strip along a chord of the disk. For a mirror radius of $r = 7.5$ cm and a rotational frequency of 8000 min^{-1}, the velocity at the circumference is 70 m/s, corresonding to an energy shift of $\Delta E =$ 3 meV. Due to the linear velocity gradient across the disk, the finite width δx of the incident beam leads to an energy width $\delta E = \Delta E \delta x / x$. (This corresponds to the dispersive broadening in crystal X-ray optics due to the angular spread of the incident

radiation.) For a beam width of $\Delta x = 1$ mm reflected at a transverse displacement of $x = 7$ cm, one obtains an energy spread of $\delta E = 80$ μeV, corresponding to a relative energy resolution of $\Delta E/\delta E = 50$. This can be improved by focusing the incident radiation to a smaller spot at the location of the mirror.

5. Rotating mirror spectrometer

5.1. Instrumentation

The schematic setup of the rotating-mirror spectrometer is shown in figure 7. The reflecting layer system consists of 11 nm ^{57}Fe on 20 nm Pd, coated on an annular region of a superpolished disk close to its circumference. The ^{57}Fe film is magnetized by a permanent-magnet structure that produces an almost homogeneous field along the footprint of the beam with a strength of approximately 50 mT. The mirror is mounted on an air lubricated bearing that provides an angular accuracy during rotation of better than 10 μrad. The surface normal of the mirror was adjusted parallel to the rotation axis with about the same angular accuracy by employing interferometric techniques. In

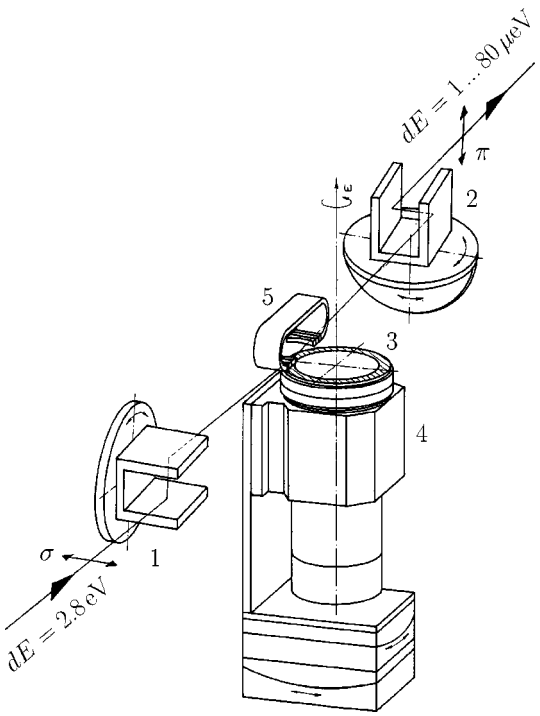

Figure 7. Schematic setup of a spectrometer for μeV-resolved X-ray scattering based on elastic nuclear resonant scattering. 1: Si(8 4 0)-polarizer; 2: Si(8 4 0)-analyzer; 3: superpolished mirror coated with ^{57}Fe; 4: drive for mirror rotation with up to 8000 min^{-1}; 5: permanent magnet for magnetization of the Fe-film parallel to $\vec{k}_0$. Polarizer and analyzer are channel-cut crystals with scattering planes tilted by 90° (crossed polarizers).

order to reach rotational frequencies of up to 8000 min^{-1}, the mirror has to be carefully balanced. With the magnetic field used here, no warming of the mirror holder due to eddy currents could be detected during rotation.

5.2. Experimental results

The spectrometer as shown in figure 7 has been characterized in an experiment carried out at the nuclear-resonance beamline ID18 [31] of the ESRF [32]. The experimental results are summarized in figure 8. Figure 8(a) shows the rocking curve of the $\sigma \rightarrow \pi$ reflectivity $|R_{\sigma\pi}(\varphi)|^2$. It was recorded by counting delayed quanta in the time window 2–100 ns. Since $R_{\sigma\pi}$ vanishes off resonance, the time spectrum $|R_{\sigma\pi}(t)|^2$ starts with zero intensity at $t = 0$. Therefore, the measured signal is equivalent to the energy integrated reflectivity and can be directely compared with curve (b) in figure 4.

As expected, the reflectivity peaks at approximately 4.0 mrad, close to the critical angle of the Pd substrate layer. The solid line is a theoretical simulation according to the theory described in [21]. Here the maximum integrated reflectivity is $50\,\Gamma_0$. The deviation from the expected value of $65\,\Gamma_0$ is caused by boundary roughness and layer inhomogeneities. Based on this value, a throughput in the range 10^4–10^5 can be expected at undulator beamlines of 3rd generation synchrotron radiation sources.

Figures 8(b), (c) display the time response of the reflection at an angle of incidence of 4.0 mrad. The decay is strongly speeded up compared to the natural decay that is represented by the straight line in figure 8(b). The intensity at late times has important implications for the signal-to-background ratio in future experiments, as will be discussed in section 5.3. Figure 8(c) shows the time response at a rotational frequency of 8000 min^{-1}. Due to the Lighthouse Effect the signal at late times is significantly suppressed: Delayed quanta are deflected by 0.1 $\mu\mathrm{rad\,ns}^{-1}$, so that with increasing time they fall out of the angular acceptance of the analyzer.

Figure 8(d) displays the time spectrum recorded at 5.4 mrad and a rotational frequency of 8000 min^{-1}. The angle of incidence is far beyond the critical angle, so that dynamical scattering effects can be neglected. Correspondingly, the speedup is strongly reduced. The shape of the quantum beat spectrum indicates that the film is indeed magnetized parallel to $\vec{k}_0$, even at the maximum rotational speed.

Finally, the energy tunability of the reflected radiation was demonstrated. A stationary reference absorber, a 11.3 μm thick ^{57}Fe foil magnetized in 45°-geometry, was introduced between polarizer and analyzer. This is another scattering geometry in which the incident polarization is not an eigenpolarization and strong $\sigma \rightarrow \pi$ conversion takes place. The energy spectra of the ^{57}Fe reference foil and the Doppler shifter are shown schematically in figure 8(e), shifted relative to each other by ΔE. The energy spectrum of the Doppler shifter is displaced by ΔE from the signal of the ^{57}Fe reference foil. The fine structure in each energy spectrum is caused by the magnetic hyperfine interaction in the scatterers. Time spectra, recorded for various values of ΔE, are shown in figures 8(b)–(f). They exhibit an overall envelope that corresponds to the incoherent superposition of the signals from the ^{57}Fe reference foil

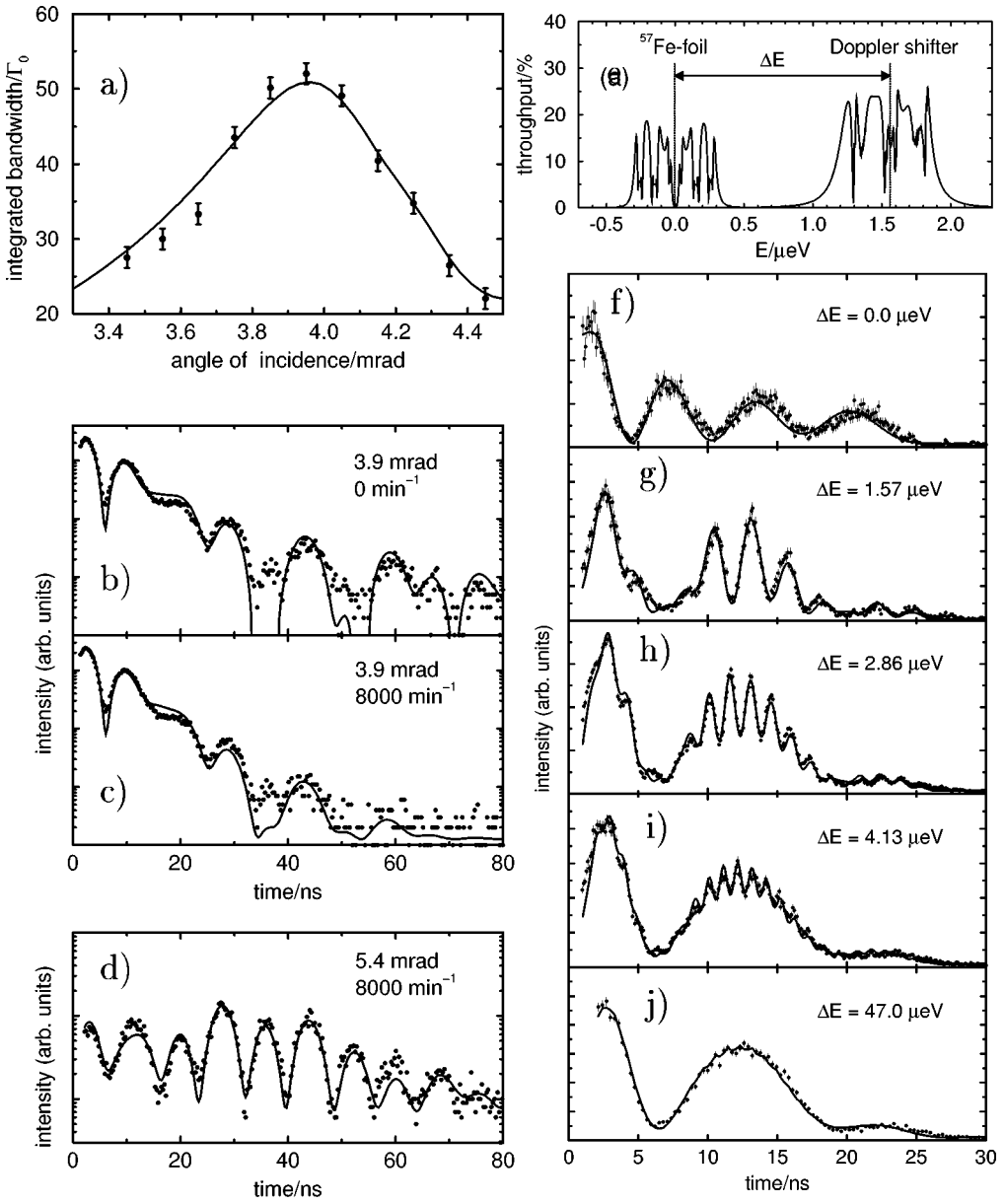

Figure 8. Characterization of the rotating-disk spectrometer. (a) Rocking curve of the energy-integrated $\sigma \rightarrow \pi$ reflectivity of the ^{57}Fe/Pd film, recorded with delayed quanta in a time window from 1 ns to 300 ns. (b) Time spectra of the ^{57}Fe/Pd film at 3.9 mrad with the mirror rotating at 0 and 8000 min^{-1}, indicating the influence of the Lighthouse Effect at late times. (c) Time spectrum of the ^{57}Fe/Pd film at 5.4 mrad and 8000 min^{-1}, showing that the magnetization is parallel to $\vec{k}_0$. (d) Energy response of $\sigma \rightarrow \pi$ scattering of the reference absorber (9 μm ^{57}Fe foil) and the ^{57}Fe layer on the rotating mirror, tuned to an energy shift ΔE. (e) Time spectra at various energy shifts ΔE between the signals from the ^{57}Fe foil and the Doppler shifter. Solid lines are theoretical simulations.

and the Doppler shifter and higher-frequency oscillations arising from the coherent interference of the two signals. The period ΔT of the oscillations is inversely proportional to the energy shift ΔE: $\Delta T = h/\Delta E$ with $h = 4.13$ μeV ns. The solid lines are calculations in which the energy shift between both signals was calculated from the angular velocity ω and the displacement x of the beam from the center of the disk. The transmission through the foil is taken into account by inserting into eq. (4.3) the (2×2) matrix that describes nuclear resonant forward scattering. An energy averaging has been carried out corresponding to the width of $\Delta x = 2$ mm of the incident beam. The time spectrum in figure 8(f) was measured with the disk at rest, showing an oscillation period of 6.8 ns that corresponds to the separation of the dominant lines in the energy spectrum. Figures 8(c)–(f) show the time spectra, measured at increasing rotational speed of the Doppler shifter. The smallest observed oscillation period of 1 ns in figure 8(i) corresponds to an energy shift of 4.13 μeV. The data in figure 8(j) were recorded at a rotational frequency of 145 min^{-1}, corresponding to an energy shift of 47 μeV. Due to the finite time resolution of the detector, the time spectrum appears as the incoherent superposition of the time spectra from the foil and the film alone.

5.3. Perspectives for inelastic spectroscopy

The radiation leaves this spectrometer with an energy bandwidth of 1–80 μeV and a tunability of ±3 meV around the 14.4 keV resonance of ^{57}Fe. First applications will be in inelastic nuclear resonant scattering from samples containing ^{57}Fe: phonon spectra are obtained by monitoring the yield of delayed fluorescence photons while the energy of the incident radiation is tuned, see, e.g., [7–10]. This means that time discrimination techniques have to be applied for detection of inelastic events. This requires that the incident radiation should exhibit a pulse-like time structure to define the time of excitation. In this spectrometer, however, this condition is deteriorated due to the fact that the radiation is generated in a nuclear scattering process. In spite of the strong speedup, the intensity at late times may generate background events in the order of the inelastic signal. On the other hand, the Nuclear Lighthouse Effect leads to a reduction of those late quanta and therefore is a welcome background suppression.

For an estimate of the countrates that can be expected in future experiments, the delayed fluorescence yield has to be calculated. The flux of K-fluorescence photons emitted in the full solid angle is given in [8]:

$$I(E) = I_0 \rho \sigma \frac{\eta_K \alpha_K}{1+\alpha} \frac{\pi}{2} \Gamma_0 S(E) =: C I_0 S(E), \tag{5.1}$$

where σ is the nuclear resonance cross-section, η_K is the K-fluorescence yield, α and α_K are the total and partial coefficients of internal conversion and Γ_0 is the natural linewidth. $C = 1.4 \cdot 10^{-6}$ eV in the case of ^{57}Fe. I_0 is the incident flux on the sample and $S(E)$ is the absorption probability per unit of energy. Values for $S(E)$ of 10–100 $(\mathrm{eV})^{-1}$ can be found in materials with low-energy excitations [14]. Taking into account corrections for absorption in the sample, as well as coverage of solid angle and detector

efficiency, one arrives at count rates of 0.1–1 s^{-1}. These values have to be compared with the flux of background events that arise predominantly from photoelectric absorption of delayed incident photons. Since the time response of this spectrometer is fast compared to the natural decay, the background can be substantially reduced by proper time gating. Ratios of 10^{-6}–10^{-7} can be achieved between the number of quanta emitted for $t > 60$ ns and the total photon flux delivered by this spectrometer. A further increase in flux of almost an order of magnitude can be gained if the collimation of the source can be matched to the angular acceptance of the polarizer/analyzer of $\approx 10 \times 10$ μrad^2.

6. Lighthouse spectrometer

6.1. Instrumentation

The crucial point in this kind of spectrometer is a high-speed rotational motion with frequencies beyond 10 kHz. High-speed rotational motion with frequencies of several kHz is commonly used in the magic-angle-spinning (MAS) technique of solid state NMR [33,34]. The samples are contained in hollow rotor cylinders consisting of sintered ceramics such as Si_3N_4 (4 mm diameter, 0.5 mm wall thickness). These rotors are terminated with a cap that is formed as a little turbine wheel. The bearing of the rotors is performed by pressurized air. The rotors are driven by jets of air that are directed to the turbine-wheel cap. The maximum rotational frequency is limited by the mechanical properties (elastic modulus, tensile strength) of the rotor material and the velocity at the circumference compared to the velocity of sound in the bearing gas. The upper limit in commercially available systems is presently 35 kHz [35]. These systems can easily be modified for X-ray transmission.

The first experiment with such a rotor system was performed at the beamline BW4 at HASYLAB (DESY, Hamburg) [36]. The experimental setup is shown schematically in figure 9. The sample was a 2.6 μm thick polycrystalline α-^{57}Fe foil, wrapped along the inner circumference of the rotor cylinder. 14.4 keV radiation was monochromatized

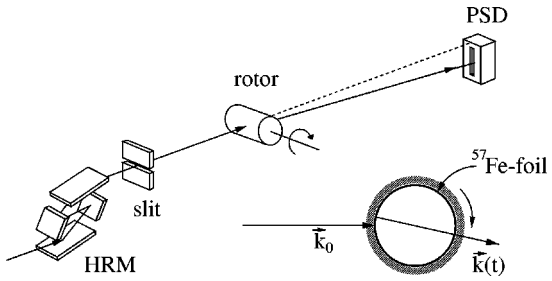

Figure 9. Experimental setup at beamline BW4 of HASYLAB for observation of the Nuclear Lighthouse Effect with high-resolution monochromator (HRM), rotor and position-sensitive detector (PSD). The scattered beam from the rotor was guided through an evacuated flight tube to the detector. In the bottom right a cross-sectional view of the scattering from the rotor is shown.

to an energy width of 6.5 meV by a high-resolution nested monochromator employing Si(4 2 2) and Si(12 2 2) reflections. The beam cross-section was 1 mm (vertical) × 2 mm (horizontal). After transmission through the rotor, the beam was guided through a 4 m long evacuated flight tube to minimize small angle scattering in air. The scattered radiation was measured with a one-dimensional position sensitive detector based on a wire proportional counter with a sensitive length of 50 mm.

6.2. Experimental results

The angular distribution of the radiation scattered from the sample rotating at 15 kHz is shown in figure 10. This rotational frequency leads to a deflection of delayed quanta with a rate of 94 μrad/ns. The quantum beats of nuclear resonant forward scattering are clearly visible on top of a background that results mainly from small angle scattering at the rotor material. The angular distribution of the background was measured independently with the energy tuned off resonance. This background was subtracted from the data to obtain the time spectrum of resonant scattering from the ^{57}Fe foil, which is shown in the inset of figure 10. The data were evaluated according to eq. (4.6) with $|\vec{A}_0(t)|^2$ calculated according to the theory of nuclear resonant forward scattering [37]. The solid line is a simulation with a foil thickness of 2.6 μm and $\Theta_s = 10^{-5}$. Remarkably, even though the radiation passes the Fe foil twice, only the single thickness contributes to the scattering. This is a consequence of an interference between different parts of the nuclear exciton that belong to the front foil, the back foil and the system of both foils [38].

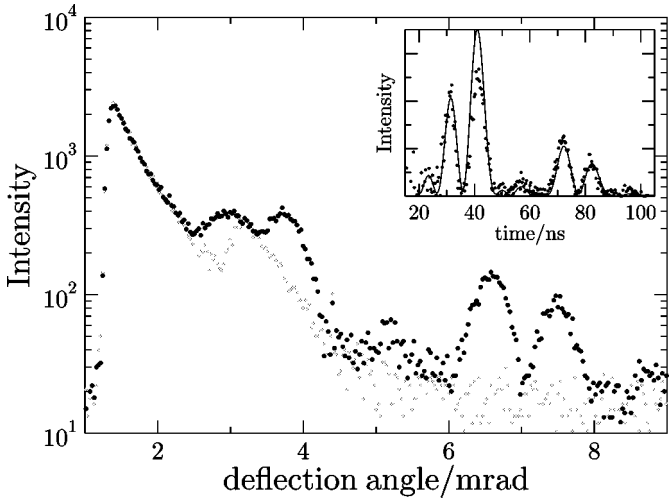

Figure 10. Measured angular distribution of 14.4 keV photons resonantly scattered from a 2.6 μm thick ^{57}Fe foil rotating at 15 kHz. The resonant scattering from the Fe foil appears on top of the small angle scattering background (grey dots). Background subtraction yields the time spectrum shown in the insert. The solid line corresponds to a simulation assuming nuclear forward scattering from a 2.6 μm Fe foil.

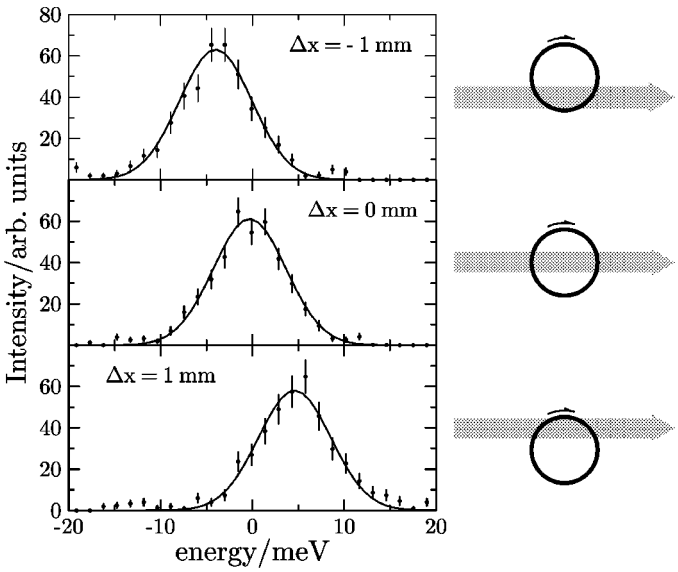

Figure 11. Energetic tuning of the deflected radiation by variation of the displacement Δx of the rotor relative to the beam.

The linear velocity at the circumference of the rotor is 140 ms^{-1}, resulting in a tunability range of ± 6.8 meV around the resonance. Energy shifts in that range can be measured with the high-resolution monochromator used in this experiment. An avalanche photodiode (APD) was placed at a fixed position to record only delayed deflected quanta. Then the count rate at the APD was monitored while the energy of the high-resolution monochromator was tuned. The result of these scans is shown in figure 11 for offsets $\Delta x = -1$, 0 and $+1$ mm relative to the center of rotation, clearly demonstrating the corresponding energy shifts of -4.5, 0.0 and $+4.5$ meV, respectively.

6.3. Inelastic spectroscopy and further applications

With respect to future inelastic scattering experiments, basically the same considerations as mentioned in section 5.3 apply.

With the lighthouse spectrometer a flux of 2000 s^{-1} has been obtained by selecting the strong quantum beat around 40 ns, using a 6 μm thick ^{57}Fe foil. Intensity losses are mainly caused by absorption in the rotor material, especially at low photon energies. This could be overcome by designing rotor materials out of low-Z materials that are able to withstand high rotational frequencies. Presently, the transmission geometry is better suited for high-energy transitions. In that case, however, the rotor with the sample has to be cooled to compensate for the reduced Lamb–Mössbauer factor at high energies. For the existing rotor systems cooling schemes down to liquid-nitrogen temperatures are available; the development to cool to liquid-helium temperatures may be a bigger effort, but not impossible.

Unwanted background in this kind of spectrometer is produced by small-angle scattering from the rotor material. This can be significantly reduced by using rotors made of single-crystalline material such as Al_2O_3 (saphire), as has been demonstrated in a recent experiment [38]. If microfocused beams can be used, then one may even think of grazing incidence reflection from mirrors that are attached to one face of the rotor. In that case small-angle scattering may be considerably less and one may even think of applying this technique to very low-energy transitions such as those of ^{181}Ta (6.5 keV) and ^{169}Tm (8.4 keV).

Moreover, the Nuclear Lighthouse Effect exhibits properties that appear to be very attractive also for *elastic* nuclear resonant scattering of synchrotron radiation:

- Since the deflection angle of resonantly scattered quanta depends only on the time difference between excitation and reemission, time resolved measurements do not require a specific bunch pattern in the storage ring. Time spectra can be recorded with a position sensitive detector without time discrimination techniques. This is of great practical importance since the machine operation of 3rd generation storage rings favors bunch patterns that do not permit time resolved measurements with good time resolution.
- With sufficient suppression of small-angle scattering from the rotor material no high-resolution crystal optics is necessary. This has been demonstrated in a recent experiment performed at the APS (Argonne, USA), where the direct beam from the heat-load monochromator was used to record spatially resolved time spectra on image plates [38]. Perhaps not even a high-heat-load monochromator will be required in future experiments. The rotor may be cooled directly by using He as bearing gas. This may be attractive for application at future radiation sources like the X-ray free-electron laser (XFEL).
- Due to negligible photoabsorption in the rotor material, the method is especially attractive for use with high-energy transitions.
- The time resolution is achieved by purely geometric means and is therefore, in contrast to other detector types, independent of the energy of the radiation. Due to the high rotational speeds, time resolutions can be achieved that are not possible with conventional techniques. The maximum rotational frequency of commercially available rotor systems is 35 kHz. This corresponds to an angular velocity of 200 $\mu\mathrm{rad\,ns}^{-1}$. With an angular resolution of 20 μrad one obtains a time resolution of 100 ps. This would be suitable for investigation of nuclear resonances with very short quantum beats or very short lifetimes. In a recent experiment, for example, the Lighthouse Effect has been used to detect excitation of the 22.5 keV resonance of ^{149}Sm ($\tau_0 = 7.5$ ns) with synchrotron radiation [38].

7. Summary and outlook

Two new techniques for inelastic X-ray spectroscopy with μeV resolution have been described. Energy tuning is based on the Doppler effect that occurs upon resonant

X-ray scattering in rotating frames. The resonantly scattered radiation is separated from the huge nonresonant background by a polarization filtering technique or the Nuclear Lighthouse Effect. In both cases, energy shifts of several meV can be achieved, as was demonstrated in the case of the 14.4 keV resonance of ^{57}Fe. Due to the radial velocity gradient in rotating systems, the energy resolution is mainly determined by the transverse dimension of the incident beam. Thus, typical energy resolutions at undulator beamlines of 3rd generation sources are in the range of a few 10 μeV. These values can be considerably improved by focusing optics.

Up to now, however, inelastic scattering experiments with these spectrometers were hampered by flux limitations. In a recent experiment at the APS, a total delayed flux of 5000 s^{-1} has been achieved. The biggest intensity loss is due to the angular acceptance in the polarizer/analyzer setup of the rotating-disk spectrometer, and absorption in the rotor material of the lighthouse spectrometer, which both amount to about a factor of 10 at 14.4 keV. If this can be overcome, then there is a realistic chance to obtain vibrational spectra with μeV resolution in reasonable time. The flux values obtained so far can certainly be increased if stronger beams from advanced insertion devices are available, up to the most powerful X-ray beams that will be generated on earth: the X-ray free electron laser (XFEL) will exceed the strongest undulator sources currently operational by orders of magnitude in peak- and average brilliance. The Lighthouse Effect may be suited for filtering an ultranarrow band out of such intense radiation, since in principle no other optical elements are needed that have to withstand the enormous heat load.

Acknowledgements

The rotating-disk spectrometer was developed at the University of Hamburg in the group of E. Gerdau, in collaboration with groups at the APS (E.E. Alp, T.S. Toellner, W. Sturhahn) and the ESRF (R. Rüffer, A.I. Chumakov). We acknowledge the continuous support of the late Prof. M. Harsdorff, Institute of Applied Physics, University of Hamburg, during preparation of the coatings. The lighthouse spectrometer was developed at the University of Rostock in the group of E. Burkel with participation of A. Bernhard, K.W. Quast and the assistance of O. Leupold and E. Gerdau. We acknowledge the kind and effective cooperation of the companies Carl Zeiss (Oberkochen, Germany), Kugler (Salem, Germany), and Bruker (Rheinstetten, Germany) during preparation of the experiments. The work at Argonne was supported by US-DOE, BES Materials Science, under contract No. W-31-109-ENG-38. The projects were supported by the German Bundesministerium für Bildung und Forschung (BMBF) under contracts No. 05 5GUAAI6 and 05 643HRA 5, and by ESRF under contract CL 0055.

References

[1] E. Burkel, *Inelastic Scattering of X-Rays with Very High Energy Resolution* (Springer, New York, 1991).
[2] E. Burkel and H. Sinn, J. Phys. Condens. Matter A 6 (1994) 225.
[3] F. Sette, G. Ruocco, M. Krisch, U. Bergmann, C. Masciovecchio, V. Mazzacurati, G. Signorelli and R. Verbeni, Phys. Rev. Lett. 75 (1995) 850.
[4] G. Ruocco, F. Sette, U. Bergmann, M. Krisch, C. Masciovecchio, V. Mazzacurati, G. Signorelli and R. Verbeni, Nature (London) 379 (1996) 521.
[5] H. Sinn, F. Sette, U. Bergmann, C. Halcoussis, M. Krisch R. Verbeni and E. Burkel, Phys. Rev. Lett. 78 (1997) 1715.
[6] C. Masciovecchio, G. Monaco, G. Ruocco, F. Sette, A. Cunsolo, M. Krisch, A. Mermet, M. Soltwisch and R. Verbeni, Phys. Rev. Lett. 80 (1998) 544.
[7] M. Seto, Y. Yoda, S. Kikuta, X.W. Zhang and M. Ando, Phys. Rev. Lett. 74 (1995) 3828.
[8] W. Sturhahn, T.S. Toellner, E.E. Alp, X. Zhang, M. Ando, Y. Yoda, S. Kikuta, M. Seto, C.W. Kimball and B. Dabrowski, Phys. Rev. Lett. 74 (1995) 3832.
[9] A.I. Chumakov, R. Rüffer, H. Grünsteudel, H.F. Grünsteudel, G. Grübel, J. Metge, O. Leupold and H.A. Goodwin, Europhys. Lett. 30 (1995) 427.
[10] A.I. Chumakov and W. Sturhahn, this issue, section V-1.1.
[11] T.M. Mooney, T.S. Toellner, W. Sturhahn, E.E. Alp and S.D. Shastri, Nucl. Instrum. Methods A 347 (1994) 348.
[12] T.S. Toellner, M.Y. Hu, W. Sturhahn, K. Quast and E.E. Alp, Appl. Phys. Lett. 71 (1997) 2112.
[13] T.S. Toellner, this issue, section VI-1.
[14] W.A. Phillips, ed., *Amorphous Solids: Low Temperature Properties* (Springer, Berlin, 1981);
F.J. Bermejo, A. Criado and J.L. Martinez, Phys. Lett. A 195 (1994) 236;
D. Caprion, P. Jund and R. Jullien, Phys. Rev. Lett. 77 (1996) 675.
[15] R. Röhlsberger, T.S. Toellner, W. Sturhahn, K.W. Quast, E.E. Alp, A. Bernhard, E. Burkel, O. Leupold and E. Gerdau, Phys. Rev. Lett. (in press).
[16] J.P. Hannon and G.T. Trammell, Physica B 159 (1989) 161.
[17] L.I. Schiff, *Quantum Mechanics*, 3rd ed. (McGraw-Hill, New York, 1986).
[18] T.S. Toellner, E.E. Alp, W. Sturhahn, T.M. Mooney, X. Zhang, M. Ando, Y. Yoda and S. Kikuta, Appl. Phys. Lett. 67 (1995) 1993.
[19] D.P Siddons, J.B. Hastings, U. Bergmann, F. Sette and M. Krisch, Nucl. Instrum. Methods B 103 (1995) 371.
[20] E.E. Alp et al., this issue, section VII-1.
[21] R. Röhlsberger, this issue, section IV-1.3.
[22] R. Röhlsberger, Ph.D. thesis, Internal Report, DESY, HASYLAB 94-06 (December 1994).
[23] A. Krol, C.J. Sher and Y.H. Kao, Phys. Rev. B 38 (1989) 8579.
[24] Y. Wang, M. Bedzyk and M. Caffrey, Science 258 (1992) 775.
[25] Y.P. Feng, S.K. Sinha, H.W. Deckman, J.B. Hastings and D.P. Siddons, Phys. Rev. Lett. 71 (1993) 537.
[26] T.S. Toellner, Ph.D. thesis, Northwestern University, Evanston, IL, USA (1996).
[27] L. Mandel and E. Wolf, *Optical Coherence and Quantum Optics* (Cambridge Univ. Press, Cambridge, 1995).
[28] M. Born and E. Wolf, *Principles of Optics*, 7th ed. (Pergamon, New York, 1978).
[29] S.K. Sinha, M. Tolan and A. Gibaud, Phys. Rev. B 57 (1998) 2740.
[30] A.Q.R. Baron, A.I. Chumakov, H.F. Grünsteudel, H. Grünsteudel, L. Niesen and R. Rüffer, Phys. Rev. Lett. 77 (1996) 4808.
[31] R. Rüffer and A.I. Chumakov, Hyp. Interact. 97/98 (1996) 589.
[32] R. Röhlsberger, E. Gerdau, R. Rüffer, W. Sturhahn, T.S. Toellner, A.I. Chumakov and E.E. Alp, Nucl. Instrum. Methods A 394 (1997) 251.

[33] F.D. Doty and P.D. Ellis, Rev. Sci. Instrum. 52 (1981) 1868.
[34] F.D. Doty, in: *Encyclopedia of Magnetic Resonance*, eds. D.M. Grant and R.K. Harris (Wiley, Chichester, UK, 1996) p. 4475.
[35] Bruker Analytical GmbH, Germany, private communication.
[36] R. Röhlsberger, A. Bernhard, E. Burkel, K.W. Quast, O. Leupold and E. Gerdau, HASYLAB Annual Report (1997).
[37] W. Sturhahn and E. Gerdau, Phys. Rev. B 49 (1994) 9285.
[38] R. Röhlsberger et al., to be published.